VIP Carbon Nanotubes Very Important Paper

How to cite: *Angew. Chem. Int. Ed.* **2020**, *59*, 18774–18785
International Edition: doi.org/10.1002/anie.202005081
German Edition: doi.org/10.1002/ange.202005081

Dynamic Covalent Formation of Concave Disulfide Macrocycles Mechanically Interlocked with Single-Walled Carbon Nanotubes

Bugga Balakrishna, Arjun Menon, Kecheng Cao, Sebastian Gsänger, Sebastian B. Beil, Julia Villalva, Oleksandr Shyshov, Oliver Martin, Andreas Hirsch, Bernd Meyer, Ute Kaiser, Dirk M. Guldi, and Max von Delius**

Abstract: *The formation of discrete macrocycles wrapped around single-walled carbon nanotubes (SWCNTs) has recently emerged as an appealing strategy to functionalize these carbon nanomaterials and modify their properties. Here, we demonstrate that the reversible disulfide exchange reaction, which proceeds under mild conditions, can install relatively large amounts of mechanically interlocked disulfide macrocycles on the one-dimensional nanotubes. Size-selective functionalization of a mixture of SWCNTs of different diameters were observed, presumably arising from error correction and the presence of relatively rigid, curved π-systems in the key building blocks. A combination of UV/Vis/NIR, Raman, photoluminescence excitation, and transient absorption spectroscopy indicated that the small (6,4)-SWCNTs were predominantly functionalized by the small macrocycles* $\mathbf{1_2}$*, whereas the larger (6,5)-SWCNTs were an ideal match for the larger macrocycles* $\mathbf{2_2}$*. This size selectivity, which was rationalized computationally, could prove useful for the purification of nanotube mixtures, since the disulfide macrocycles can be removed quantitatively under mild reductive conditions.*

Introduction

More than two decades after their discovery,[1] single-walled carbon nanotubes (SWCNTs) have found impressive laboratory uses as one-dimensional, nanoscopic (semi)conductors of electric current.[2] However, large-scale applications of these synthetic carbon allotropes will most likely require further advances in (supramolecular) chemistry. For instance, it is still not possible to prepare large quantities of monodisperse, that is, chirality-pure, SWCNTs either by seeded synthesis or by separation of mixtures, despite recent progress.[3] Moreover, rendering SWCNTs solution-processable by chemical functionalization can be problematic,[4] because any covalent functionalization partially destroys the appealing optoelectronic properties of the nanotubes,[5] while noncovalent approaches suffer from poor stability and/or longevity.[6]

An appealing solution to the functionalization problem is to "wrap" oligomeric/polymeric helices (oligonucleotides, π-extended polymers, or peptides) around SWCNTs.[7] A potential solution to both the functionalization and the purification problem is to form numerous discrete macrocycles around SWCNTs (Figure 1), effectively turning the SWCNT into a poly[*n*]rotaxane.[8] This approach has been pioneered by Pérez and co-workers who have formed various types of macrocycles by irreversible ring-closing olefin metathesis around SWCNTs that acted as templates (Figure 1 a).[9] Pérez and González-Rodríguez have recently also described the formation of hydrogen-bonded squares around SWCNTs (Figure 1 b)[10] and Ohe reported the "threading" of a shape-persistent conjugated macrocycle onto SWCNTs of matching diameter (Figure 1 c).[11] First reports on remarkable catalytic properties of such "mechanically interlocked nanotube" (MINT) materials have appeared recently.[12]

[*] Dr. B. Balakrishna, Dr. S. B. Beil, J. Villalva, O. Shyshov, Prof. Dr. M. von Delius
Institute of Organic Chemistry, Ulm University
Albert-Einstein-Allee 11, 89081 Ulm (Germany)
E-mail: max.vondelius@uni-ulm.de

A. Menon, Prof. Dr. D. M. Guldi
Department of Chemistry and Pharmacy & Interdisciplinary Center for Molecular Materials
Friedrich-Alexander University Erlangen-Nürnberg
Egerlandstrasse 3, 91058 Erlangen (Germany)
E-mail: dirk.guldi@fau.de

Dr. K. Cao, Prof. Dr. U. Kaiser
Electron Microscopy of Materials Science
Central Facility for Electron Microscopy
Ulm University
Albert-Einstein-Allee 11, 89081 Ulm (Germany)

S. Gsänger, Prof. Dr. B. Meyer
Interdisciplinary Center for Molecular Materials (ICMM) & Computer-Chemistry-Center (CCC)
Friedrich-Alexander University Erlangen-Nürnberg
Nägelsbachstrasse 25, 91052 Erlangen (Germany)

O. Martin, Prof. Dr. A. Hirsch
Department of Chemistry and Pharmacy & Joint Institute of Advanced Materials and Processes (ZMP)
Friedrich-Alexander University Erlangen-Nürnberg
Nikolaus-Fiebiger-Strasse 10, 91058 Erlangen (Germany)

Supporting information and the ORCID identification number(s) for the author(s) of this article can be found under: https://doi.org/10.1002/anie.202005081.

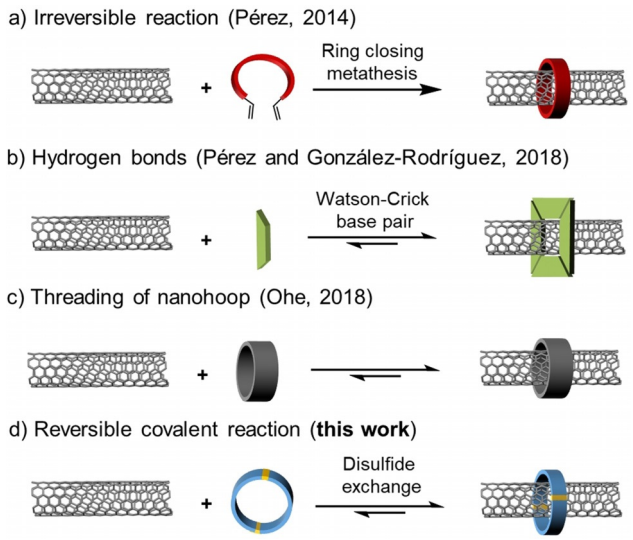

Figure 1. Approaches for the synthesis of mechanically interlocked SWCNTs.

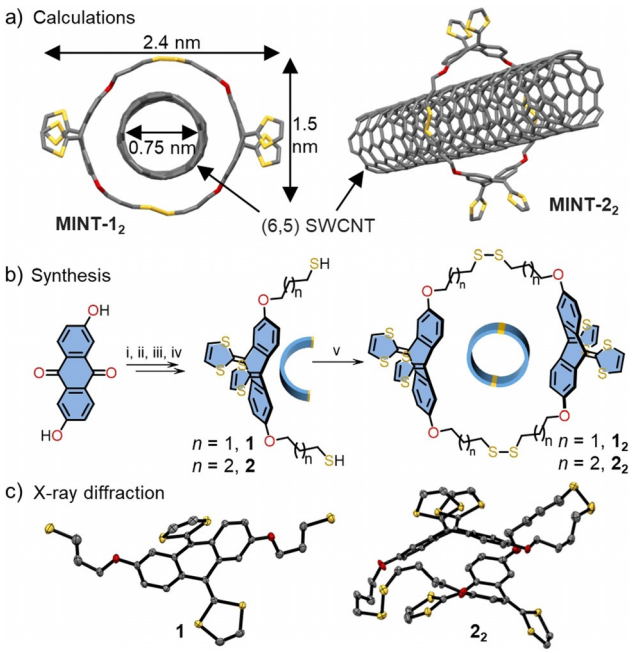

Figure 2. a) Energy-minimized (GAFF) molecular model of mechanically interlocked (6,5)-SWCNTs with different ring sizes of disulfide exTTF macrocycles. b) i) *tert*-Butylchlorodimethylsilane (4 equiv), imidazole (4 equiv) DMF, rt, 16 h, 78%; ii) dimethyl (1,3-dithiol-2-yl)phosphonate (2.5 equiv), *n*-BuLi (2.5 equiv) THF, −78 °C, 16 h, 67%; iii) TBAF (4 equiv), THF, rt, 16 h, 98%; iv) Cs_2CO_3 (4 equiv), (3-bromopropyl)-(trityl)sulfane/(4-bromobutyl) (trityl)sulfane (3 equiv), DMF, rt, 16 h, 59–65%; v) 20% TFA, *i*-Pr_3SiH, CH_2Cl_2, rt, 48 h, 73% for **1**, 42% for **2**; vi) TEA (4 equiv), I_2 (0.55 equiv), $CHCl_3$, 82% for $\mathbf{1}_2$, 53% for $\mathbf{2}_2$. c) X-ray single-crystal structures of exTTF dithiol **1** and exTTF disulfide macrocycle $\mathbf{2}_2$. ORTEP drawings with 30% probability.

Inspired by these reports, we wondered whether MINTs based on dynamic covalent macrocycles could offer a "best-of-both-worlds" scenario:[13] the reversibility of the ring-closing step could make the functionalization step more efficient thanks to internal error correction, while the ensuing poly[*n*]rotaxane construct could be as stable as that generated by means of an irreversible covalent reaction. Moreover, it should be possible to cleave the rings using the dynamic covalent bonds as the "weakest links" under mild reaction conditions, thus opening up the possibility to use this approach for the diameter-selective functionalization and sorting of SWCNT mixtures. Herein, we report that disulfide macrocycles based on the π-extended tetrathiafulvalene-(exTTF)-motif (Figure 1 d) indeed offer these advantages.[15,16] We demonstrate high functionalization degrees, the mild reductive defunctionalization of the MINTs, and an investigation into the interaction between nanotubes and rings (diameter-selectivity and charge transfer).

Results and Discussion

Design and Synthesis of Building Blocks

For the present study, we chose commercially available, (6,5) chirality enriched CoMoCAT-SWCNTs as templates, because the relatively large curvature[14] of small-diameter SWCNTs should enable strong and potentially size-selective interactions between nanotubes and suitable π-curved macrocycles. The macrocycle design was based on the concave exTTF[15] binding motif (Figure 2) and two alkyl thiol residues, which represent the key functional groups for reversible disulfide exchange reactions.[16] To identify an optimal match between macrocycles and SWCNTs, we carried out theoretical calculations based on the Generalized Amber Force Field (GAFF). By evaluation of the lengths of the alkyl spacers, we found a good induced-fit for dimeric macrocycles for $n=1$ (*n*-propyl spacer) and $n=2$ (*n*-butyl spacer) for the (6,5)-SWCNTs (Figure 2 a). The macrocycles are unstrained and the interaction with the (6,5)-SWCNT is rather strong, with observed adsorption energies of −34 kcal mol^{-1} ($n=1$) and −44 kcal mol^{-1} ($n=2$) in the gas phase (Tables S8 and S9). Molecular dynamics simulations revealed that macrocycles with longer spacers ($n>2$) are less likely to "wrap around" the SWCNTs, because the flexibility of the alkyl chains starts to outweigh the preorganization provided by the rigid exTTF motif (Figure S46).

Based on the most promising computational models, we synthesized two U-shaped dithiols (Figure 2 b, **1** and **2**) in a synthetic route comprising five linear steps (Scheme S1). The concave shape of the exTTF-motif with a bend angle of approximately 140° in the conjugated backbone becomes evident from the two solid-state structures shown in Figure 2 c. Dimeric disulfide macrocycles $\mathbf{1}_2$ and $\mathbf{2}_2$ were obtained in yields of 82% and 53%, respectively, by oxidation of the dithiols **1** and **2** (concentration: 10 mM) using iodine as a mild oxidant. This irreversible oxidation reaction did not produce observable quantities of the monomeric macrocycles $\mathbf{1}_1$ or $\mathbf{2}_1$, which suggests that these products are highly strained and are, therefore, not expected during the envisaged reversible ring formation around SWCNTs. Indeed, when $\mathbf{1}_2$ and $\mathbf{2}_2$ were rendered constitutionally dynamic in the absence of a template (by addition of 1,8-diazabicyclo[5.4.0]undec-7-ene

(DBU) as base and dithiothreitol (DTT) as reducing agent),[16] we exclusively observed the formation of the trimeric and tetrameric macrocycles (for HPLC traces and corresponding MALDI-MS spectra, see Figures S25 and S26). Molecular mechanics calculations predict that both macrocycles have flexible cavities that can accommodate SWCNTs with a diameter of up to 0.82 nm ($n=1$) and up to 1.0 nm ($n=2$; Figures 2a and S47), while these cavities collapse in the solid state to allow tight packing (Figure 2c, right).

Dynamic Covalent Functionalization of SWCNTs

Having macrocycles $\mathbf{1}_2$ and $\mathbf{2}_2$ as well as efficient conditions for disulfide exchange in hand, we tested our key hypothesis that SWCNTs could act as convex templates during the reversible covalent opening and closing of the concave rings (Figure 3a, top). Under optimized conditions, purified (6,5)-enriched (see Section 4.1 in the Supporting Information) SWCNTs (4.0 mg) were suspended in DMF (4.0 mL) by sonication and the macrocycles $\mathbf{1}_2$ or $\mathbf{2}_2$ (0.04 mmol), DBU (8 equiv), and DTT (10 mol%) were added. In all following studies the same batch of (6,5)-SWCNTs was used. During our optimization study, we found that a reaction time of 72 h was sufficient to guarantee equilibration (Table S2). The exchange reaction was quenched by addition of iodine, and the reaction mixture was filtered through a polytetrafluoroethylene (PTFE) membrane with a pore size of 0.2 μm. The collected solids were washed multiple times by suspending in dichloromethane, ultrasonication, and filtration to remove weakly adsorbed exTTF macrocycles and reagents. The so-obtained "Rev-MINT" samples (Figure 3a, top) were dried under reduced pressure and subjected to thermogravimetric analysis (TGA) to quantify the degree of functionalization (DoF). To put the obtained results into perspective, we also carried out two reference experiments under nearly identical conditions (see section 4 in the Supporting Information). In the "Irrev-MINT" experiment, we irreversibly oxidized the dithiols **1** or **2** in the presence of the SWCNTs (Figure 3a, middle),[17] and in the "Supra-MINT" experiment, we simply sonicated the macrocycles $\mathbf{1}_2$ or $\mathbf{2}_2$ together with the SWCNTs (Figure 3a, bottom).

As shown in Figure 3b (for the case of MINT-$\mathbf{2}_2$), all samples obtained by the three different experimental approaches show a significant weight loss in the TGA trace between 300 and 420 °C (Figure 3b). This loss occurs below the temperature required for the oxidative decomposition of the nanotubes (black line) and is in good agreement with results on related MINT samples described by Pérez and coworkers.[9a] To confirm that the TGA weight losses are due to the cleavage of exTTF derivatives, we carried out TG(-GC)-MS experiments. This rigorous analysis of the Rev-MINT samples indeed revealed a multitude of fragments that clearly

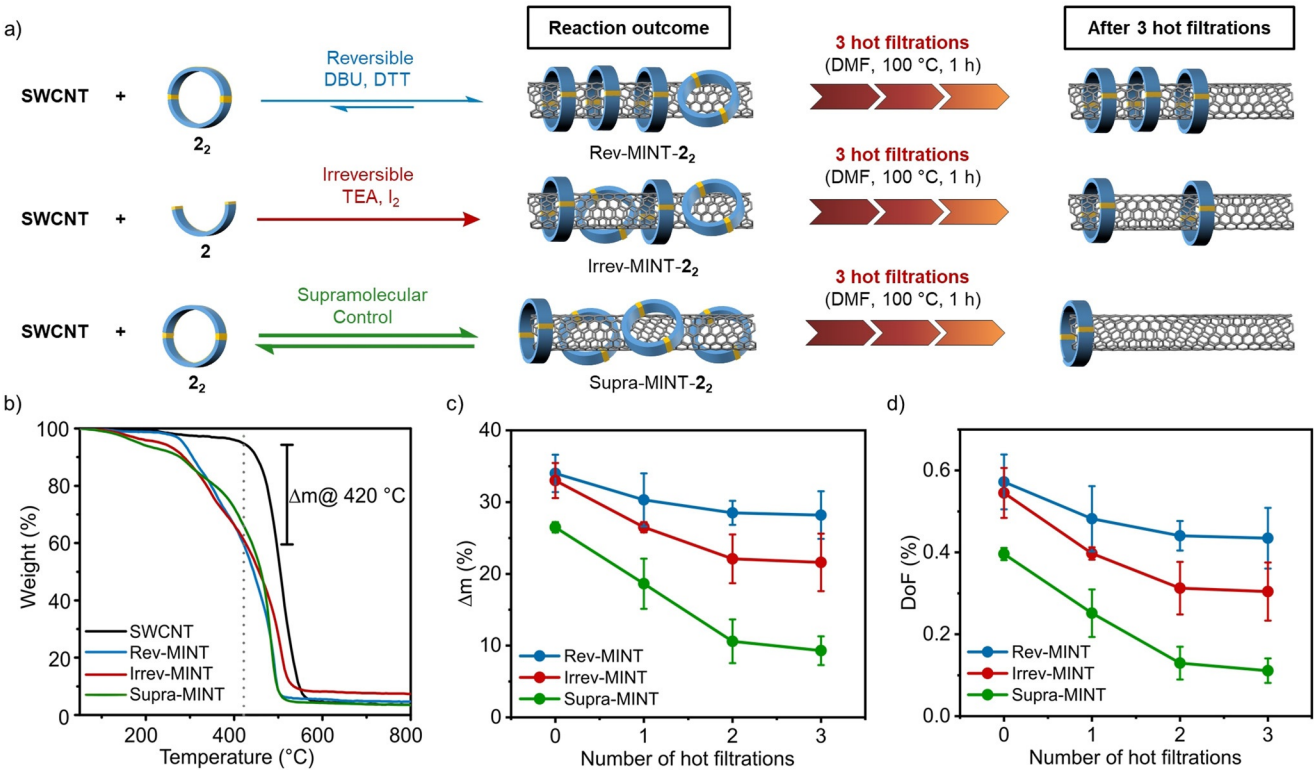

Figure 3. a) Schematic representation of different functionalization approaches of SWCNTs with $\mathbf{2}_2$ and results after three hot filtration steps. b) TGA trace of the reaction outcome (rt to 1000 °C, 10 °C min^{-1} under air) for the degree of functionalization (black: pristine SWCNTs, blue: Rev-MINT, red: Irrev-MINT and green: Supra-MINT). c) Results of TGA analysis (Δm at 420 °C) after synthesis and three consecutive hot filtration steps for the three functionalization approaches. d) Summary of the degree of functionalization of all samples according to Equation (2) after synthesis and three hot filtration steps.

originate from the exTTF moiety (see Figure S35). When comparing the TG(-GC)-MS data of Rev-MINT-$\mathbf{2_2}$ and pristine $\mathbf{2_2}$, the only notable difference was a shift of the MS peaks towards higher temperatures for the MINT samples (see Table S5), indicating that the interaction of $\mathbf{2_2}$ with the SWCNT stabilizes the macrocycles from thermolysis.

To gain deeper insights into the functionalization efficiency, we defined Δm as the fraction of TGA weight loss that can be attributed to exTTF macrocycles [Eq. (1), Figure 3b].[18] Although Δm is an intuitive figure of merit that is particularly useful for comparing experiments within this study (Figure 3c), it is not a reliable metric for comparing MINTs with macrocycles of different molar masses. Hence, we also calculated a degree of functionalization (DoF) according to Equation (2), which is routinely used to assess the covalent functionalization of SWCNTs (see section 5 in the Supporting Information). To allow comparisons with previous MINTs[9–11] and with covalently functionalized SWCNTs,[19] we report both the Δm and DoF values throughout this study. Moreover, each experiment was performed in triplicate to allow an assessment of the reproducibility of the different functionalization approaches (error bars in Figure 3c,d).

$$\Delta m\ (@420^{\circ}C) = \Delta m(\text{pristine}) - \Delta m(\text{MINT}) \quad (1)$$

$$\text{DoF}\ (\%) = \frac{m(\text{macrocycle}) \times M(C_{SWCNT})}{m(C_{SWCNT}) \times M(\text{macrocycle})} \times 100 \quad (2)$$

When performing TGA analysis immediately after the three different functionalization procedures described above, we found relatively similar Δm/DoF values for the Rev-MINT-$\mathbf{1_2}$ ($33 \pm 2\,\%/0.56 \pm 0.06\,\%$) and Rev-MINT-$\mathbf{2_2}$ ($35 \pm 3\,\%/0.57 \pm 0.07\,\%$) samples, which suggests that the ring size leads to a small, yet statistically significant difference in the reaction outcome. Similar Δm/DoF values were also observed for the Irrev-MINT-$\mathbf{2_2}$ ($33 \pm 2\,\%/0.55 \pm 0.06\,\%$) and Supra-MINT-$\mathbf{2_2}$ ($26 \pm 1\,\%/0.40 \pm 0.02\,\%$) reference experiments (Figure 3c,d).

Since we were surprised by the high Δm/DoF values observed in the Supra-MINT control experiment, where $\mathbf{2_2}$ was simply stirred for 72 h with SWCNTs, we decided to test whether the initial Δm/DoF values could be due to adsorbed, as opposed to mechanically interlocked, macrocycles. We therefore heated all samples at 100 °C for 1 h in DMF, followed by filtration through a PTFE membrane that was placed on a hot frit (ca. 70 °C), to prevent rapid re-adsorption of free macrocycles to the nanotubes on the cold filter medium. After thorough rinsing with dichloromethane and drying of the samples, TGA analyses were performed to quantify the remaining Δm/DoF values and thus determine the amount of macrocycles that were not removed during this procedure (Figure 3a, right).[20] Moreover, we performed these experiments in triplicate and repeated the hot filtration procedure three times in sequence until we reached a "plateau" for the Δm and DoF values (Figure 3c,d). We propose that the mass loss observed at the plateau level is predominantly due to the presence of mechanically interlocked rings, whose removal would require harsher conditions. As expected from an approach that features error correction,[13,16,21] TGA analysis showed that over three hot filtration cycles the Rev-MINT samples exhibit only a small decrease in the Δm and DoF values (about 5 %/0.14 %, Figure 3c,d, blue). The final Δm/DoF values of $28 \pm 3\,\%/0.43 \pm 0.07\,\%$ (Rev-MINT-$\mathbf{2_2}$), $22 \pm 4\,\%/0.30 \pm 0.07\,\%$ (Irrev-MINT-$\mathbf{2_2}$) and $9 \pm 2\,\%/0.11 \pm 0.03\,\%$ (Supra-MINT-$\mathbf{2_2}$) after three hot filtrations provide further evidence for the notion that our dynamic covalent approach produces the most robust type of non-covalent SWCNT functionalization.

Assuming that the desorption of supramolecularly bound macrocycles is nearly complete after three hot filtration cycles, we can further deduce from Figure 3c,d that the freshly prepared Rev-MINT, Irrev-MINT, and Supra-MINT samples contain ratios of 5:1, 2:1, and 1:2 of strongly and loosely bound macrocycles, respectively. We were initially surprised that the Supra-MINT samples at the plateau level still contain a non-negligible portion of strongly bound macrocycles. This result is, however, consistent with a structural proposal by Pérez,[9a,e] namely that the macrocycles in MINTs are not prevented from dethreading by terminal stoppers on the nanotubes, but instead by crossing points between several nanotubes, which can be observed by HR-TEM (Figure S42) and also seem to exist in suspension.[9a–e] In the Supra-MINT samples, some macrocycles could therefore behave like Ohe's nanohoops[11] and thread onto the non-stoppered tips of SWCNTs. These "pseudo-rotaxane"-type rings may be harder to remove than externally adsorbed ones (see Figure 3a). On the other hand, the non-negligible portion of easily removed macrocycles in the Rev-MINT samples (5 % by total weight) is arguably due to the inhomogeneous nature of the (6,5)-enriched SWCNT starting material, which besides (6,5)-SWCNTs contains significant quantities of size-mismatched SWCNTs (see below for PLE evidence).

To demonstrate that our approach is suitable for dispersing SWCNTs in organic solvents, the Rev-MINT-$\mathbf{2_2}$ sample was suspended in toluene by ultrasonication. Ultracentrifugation and removal of the solvent from the supernatant produced a pale yellowish solid. This material was successfully resuspended in tetrahydrofuran (THF), and analyzed by 3D-NIR fluorescence (Figure S37g,h). The characteristic fluorescence features at high optical density (OD 0.1) show that Rev-MINT materials form stable dispersions in organic solvent without additives.

Reductive Defunctionalization

To demonstrate that the Rev-MINT approach is in principle suitable for the purification of SWCNT mixtures, we reductively defunctionalized the MINT samples and determined the degree of (de)functionalization by HPLC analysis. We therefore treated a Rev-MINT-$\mathbf{1_2}$ sample for 48 h under ambient conditions with an excess of DTT to reduce the disulfide linkages in the dimeric $\mathbf{1_2}$ macrocycle. The product of this reaction is the monomeric dithiol **1**, which should readily desorb from the nanotubes during a filtration and washing procedure (Figure 4a,b). Indeed, when we analyzed the recovered SWCNTs by TGA, we observed

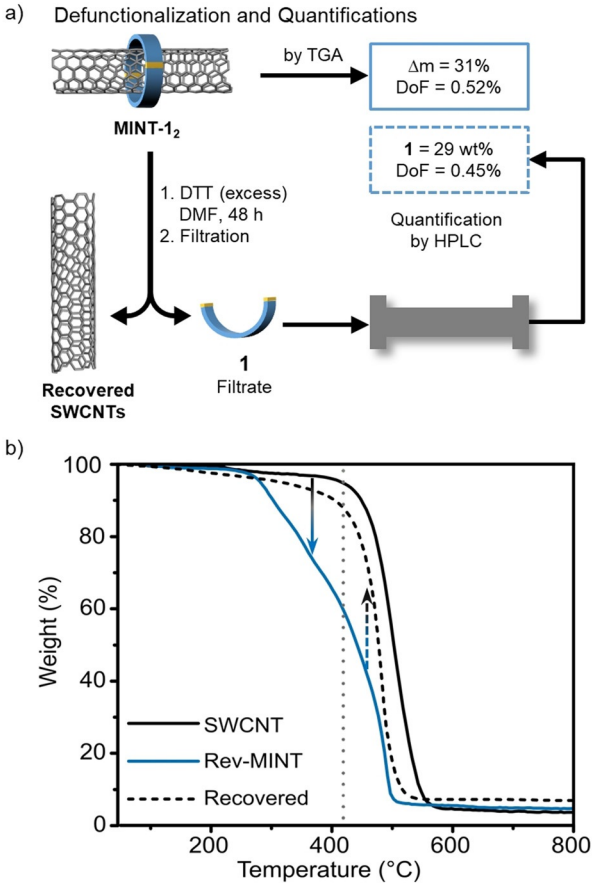

Figure 4. a) Reductive defunctionalization of MINTs to release pristine CNTs and dithiol **1**. Quantification of the defunctionalization by HPLC analysis using naphthalene as an internal standard. Weight% relative to original Rev-MINT-$\mathbf{1}_2$. b) TGA analysis of pristine CNTs (black), freshly prepared functionalized Rev-MINT-$\mathbf{1}_2$ (blue), and recovered CNTs after reductive defunctionalization of Rev-MINT-$\mathbf{1}_2$ (dotted lines).

temperature profiles very similar to those observed for the pristine SWCNT starting material (Figure 4b, dotted line vs. black line).[22] Moreover, this defunctionalization procedure allowed us to determine the degree of functionalization of MINT samples by quantifying the reduced dithiol (**1**) in the filtrate using a quantitative HPLC method (Figure 4a and Figure S36). The Δm/DoF values obtained by this method were 29%/0.45%, which are in very good agreement with the Δm/DoF values of 31%/0.52% determined by TGA. These defunctionalization studies demonstrate that our Rev-MINT approach allows the mild and quantitative recovery of both the dithiol and SWCNT starting materials.

Spectroscopic Characterization

Following the TGA-based optimization of functionalization and defunctionalization procedures, we proceeded to explore the composition of the samples as well as the interactions between macrocycles and SWCNTs by state-of-the-art spectroscopy. The absorption spectra (D_2O/SDS (1 wt%), rt) of the (6,5)-enriched SWCNT starting material (black) and the corresponding Rev-MINT-$\mathbf{1}_2$ (dark blue) as well as Rev-MINT-$\mathbf{2}_2$ (light blue) are shown in Figure 5a. Steady-state absorption spectra reveal the characteristic features of S_{22} and S_{11} transitions in the visible and near-infrared (NIR) region, respectively. For example, the most dominant absorptions of (6,5)-SWCNTs are seen at 578 and 995 nm, while those of (7,5)-SWCNTs evolve at 663 and 1022 nm. In the corresponding MINTs, all features are broadened and red-shifted to 584, 1017, 665, and 1045 nm for Rev-MINT-$\mathbf{1}_2$ as to 588, 1024, 668, and 1052 nm for Rev-MINT-$\mathbf{2}_2$. From these shifts we conclude sizeable electronic communication/interaction between exTTF macrocycles and SWCNTs already in the ground state. Notable is the fact that the S_{22} absorptions of Rev-MINT-$\mathbf{1}_2$ and Rev-MINT-$\mathbf{2}_2$ are subject to a weaker red-shift than the S_{11} absorptions.[23]

When comparing the relative absorptions of (6,5)-SWCNTs, their maxima are stronger and narrower for (6,5)-enriched SWCNTs than for all MINTs. In addition, the S_{11} and S_{22} transitions are red-shifted. These observations suggest a chiral selectivity of the exTTF-based macrocycles $\mathbf{1}_2$ and $\mathbf{2}_2$ during the formation of mechanically interlocked structures promoted by electronic interactions. Alternatively, the size of the cavity of the macrocycles might also influence the chiral selectivity towards the construction of macrocycles around SWCNTs. It should be noted that the reversible formation and breakage of exTTF disulfide bonds after MINT formation stabilizes the disulfide bond from breakage.

Raman spectroscopy is, in addition to steady-state absorption and fluorescence spectroscopies, a powerful method to inspect chiral selectivity (Figure 5b). To this end, we carefully analyzed the radial breathing modes (RBM), which are unique measures for the chirality of each SWCNT (Figure 5c). The signals, which evolve at about 262, 288, 303, and 341 cm^{-1} stem from (7,6)-, (7,5)-, (6,5)-, and (6,4)-SWCNTs, respectively. It is important to note here that the relative Raman intensities do not reflect the relative abundance of chiralities. Although the peak for the (7,5)-SWCNTs is the most intense, the (6,5)-SWCNTs are actually most abundant in the "(6,5)-enriched" starting material (41% according to the manufacturer; see Figure 6 for more representative PLE spectra). Spectral normalization with respect to the RBM intensity of (7,5)-SWCNTs points toward a significant intensity decrease of the (6,5)- and (6,4)-SWCNTs in Rev-MINT-$\mathbf{1}_2$ and Rev-MINT-$\mathbf{2}_2$ relative to the (6,5)-enriched SWCNT reference.[24] The relative (6,4)-SWCNTs RBM feature is notably weaker in Rev-MINT-$\mathbf{1}_2$ than in Rev-MINT-$\mathbf{2}_2$. At this point we exclude the presence of mechanically interlocked rings around (7,6)-SWCNTs in Rev-MINT-$\mathbf{1}_2$, as also predicted by the calculations (Figure S44). Taking the Raman experiments into consideration, selective interactions between $\mathbf{1}_2$ or $\mathbf{2}_2$, on the one hand, and small-diameter SWCNTs, on the other hand, is in line with the conclusions reached from the fluorescence experiments (see below).

Next, we turned to statistical Raman analysis as a versatile tool to shed light onto doping in the ground state. To this end, thousands of Raman spectra were recorded for each sample using 633 nm laser excitation. (6,5)-Enriched SWCNTs, Rev-MINT-$\mathbf{1}_2$, and Rev-MINT-$\mathbf{2}_2$ were dispersed in D_2O/SDS and

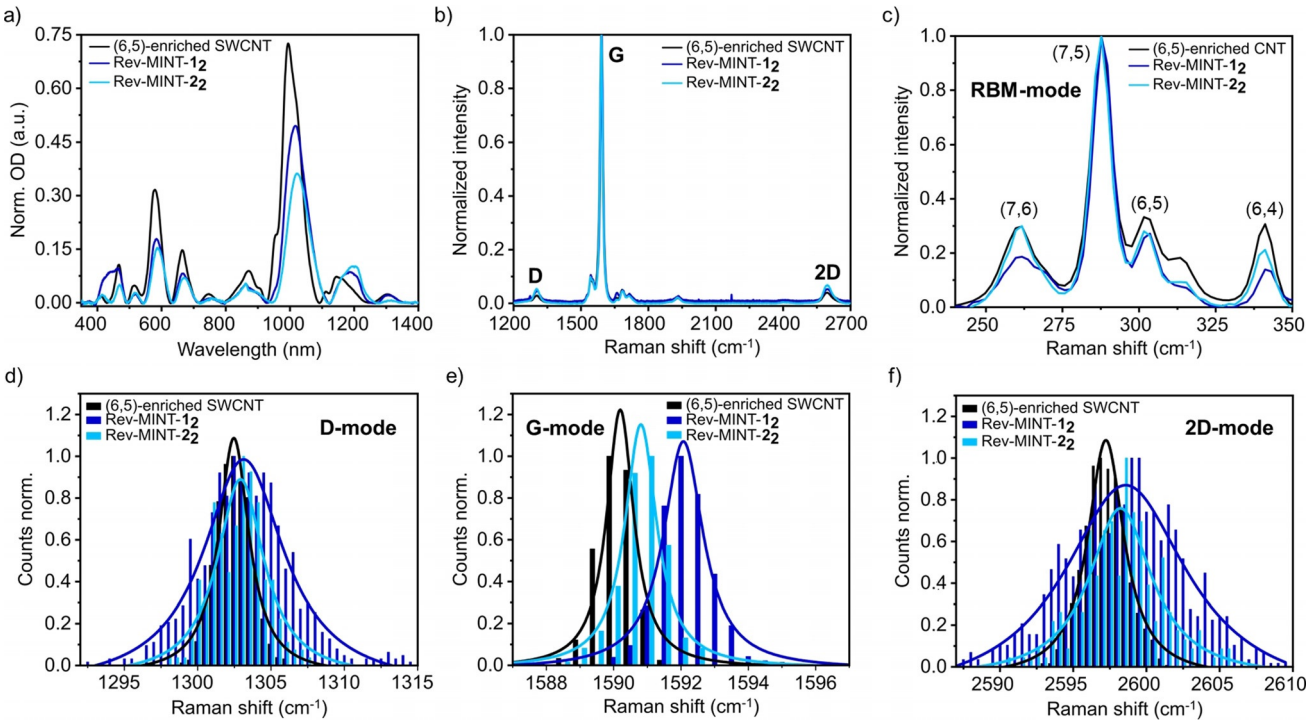

Figure 5. a) Normalized absorption spectra of (6,5)-enriched SWCNT starting material (black), Rev-MINT-$\mathbf{1}_2$ (dark blue), and Rev-MINT-$\mathbf{2}_2$ (light blue) in D_2O/SDS (1 wt%) at rt, baseline-corrected and normalized absorption at 1159 nm ((7,6)-SWCNTs absorption). b) Normalized Raman spectra showing D-, G-, and 2D-modes of drop-casted samples from D_2O/SDS suspension, with 633 nm laser excitation. c) Radial breathing modes (RBM) normalized to (7,5)-SWCNTs. Normalized statistical Raman histograms of d) D-mode, e) G-mode, and f) 2D-mode; drop-casted from D_2O/SDS suspensions with 633 nm laser excitation.

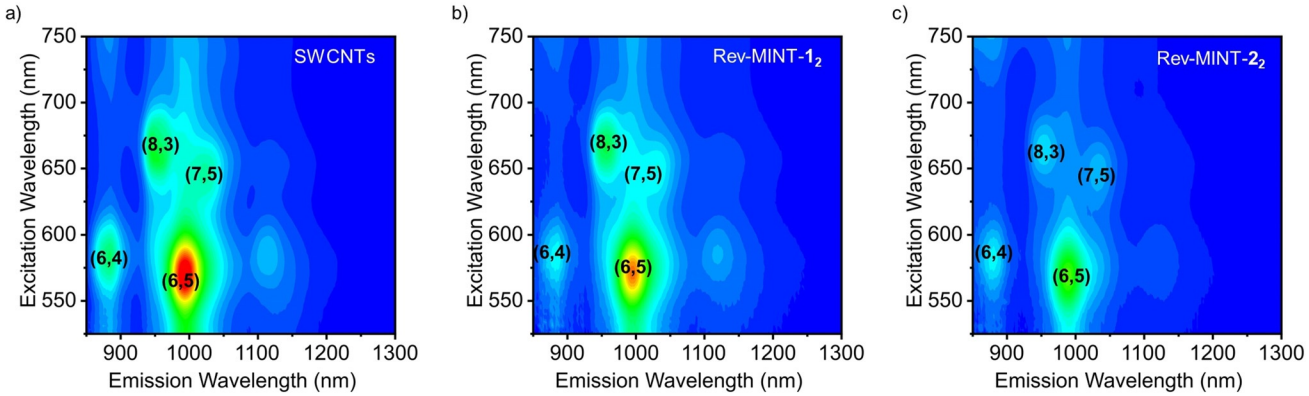

Figure 6. 3D-NIR fluorescence spectra in D_2O/SDS (1 wt%) at rt with matching absorption in the excitation range between 525 and 800 nm: a) (6,5)-enriched SWCNTs, intensities range from 0 to 500000 counts, b) Rev-MINT-$\mathbf{1}_2$, intensities range from 0 to 150000 counts, c) Rev-MINT-$\mathbf{2}_2$, intensities range from 0 to 150000 counts.

drop-casted on silicon wafers. The resulting histograms are shown in Figure 5d–f. The respective D-, G-, and 2D-modes show small up-shifts from 1302, 1590, and 2597 cm^{-1} for (6,5)-SWCNTs, to 1303, 1592, and 2598 cm^{-1} for Rev-MINT-$\mathbf{1}_2$, and to 1303, 1591, and 2598 cm^{-1} for Rev-MINT-$\mathbf{2}_2$. The presence of small up-shifts for the MINTs indicates weak charge-transfer interactions in the solid state. In this case, charge density is donated from the electron-rich exTTF moieties to the SWCNTs.[9c,f]

As a complement, cluster analyses of the (6,5)-enriched SWCNTs, Rev-MINT-$\mathbf{1}_2$, and Rev-MINT-$\mathbf{2}_2$ were carried out. The resulting Raman mean spectra are illustrated in Figure 5b. Important is the fact that the lack of significant changes in the I_D/I_G ratios when contrasting (6,5)-enriched SWCNTs (0.028), Rev-MINT-$\mathbf{1}_2$ (0.034), and Rev-MINT-$\mathbf{2}_2$ (0.048) confirms the absence of defects during the functionalization.

Insights into the excited-state interactions were obtained by analyzing the SWCNT-centered fluorescence in the NIR

region. Initially, we focused on the 3D-NIR fluorescence spectra of (6,5)-enriched SWCNTs, Rev-MINT-$\mathbf{1}_2$ and Rev-MINT-$\mathbf{2}_2$, which in the range between 850 and 1300 nm exhibit the characteristic fluorescence features illustrated in Figure 6 a–c. When using excitation wavelengths in the range of 525 and 800 nm, features for (6,4)-, (6,5)-, (8,3)-, and (7,5)-SWCNTs were observed. At first glance, a significant quenching was observed for both MINTs. A closer look reveals, however, that the decrease in the fluorescence intensity was stronger in Rev-MINT-$\mathbf{2}_2$ than in Rev-MINT-$\mathbf{1}_2$: (6,4)-SWCNTs (fluorescence quenched by 82 % relative to pristine SWCNTs), (6,5)-SWCNTs (85 %), (8,3)-SWCNTs (85 %), and (7,5)-SWCNTs (80 %) versus (6,4)-SWCNTs (83 %), (6,5)-SWCNTs (73 %), (8,3)-SWCNTs (73 %), and (7,5)-SWCNTs (68 %). This corroborates selective electronic interactions between the exTTF macrocycles and SWCNTs in their excited states.

Similar to the trend seen in the steady-state absorptions, the fluorescence features of (6,5)-enriched SWCNTs at 883, 952, 995, and 1031 nm appear red-shifted in Rev-MINT-$\mathbf{1}_2$, that is, at 886, 956, 998, and 1036 nm, while in Rev-MINT-$\mathbf{2}_2$, the trend is slightly reversed. Overall, smaller diameter SWCNTs, that is, (6,4)- and (6,5)-SWCNTs, are slightly blue-shifted to 880 and 990 nm, whereas larger diameter SWCNTs, that is, (8,3)- and (7,5)-SWCNTs, are red-shifted to 955 and 1036 nm, respectively (Figure S37 a,b). All the aforementioned results confirm the redistribution of electron density from the electron-donating exTTF moieties to the SWCNTs.[25]

Overall, these results point to a higher degree of functionalization in the case of smaller diameter SWCNTs, that is, (6,4)- and (6,5)-SWCNTs in comparison to their larger diameter analogues, namely (8,3)- and (7,5)-SWCNTs. In other words, the selective interaction as well as fluorescence quenching depends on matching the diameters of the macrocycles and SWCNTs as well as on the flexibility of the macrocycle after MINT formation (see above). Specifically, in Rev-MINT-$\mathbf{1}_2$ the strongest interactions are found between $\mathbf{1}_2$ and (6,4)-SWCNTs, whereas the interactions in Rev-MINT-$\mathbf{2}_2$ are strongest between $\mathbf{2}_2$ and (6,5)-SWCNTs. The data for $\mathbf{1}_2$ or $\mathbf{2}_2$ point towards a lack of communication with large-diameter (8,3)- and (7,5)-SWCNTs. We imply that the fluorescence quenching stems from either energy- or electron-transfer pathways, which compete with the intrinsic fluorescent deactivation.

Transient Absorption Studies

Further insights into excited-state interactions and the impact of the mechanically bound exTTF macrocycles on the excited-state dynamics of SWCNTs came from femtosecond transient absorption measurements, which were performed with an excitation wavelength of 387 nm. Representative 3D-transient spectra with the corresponding deconvoluted evolution-associated spectra (EAS), the associated population dynamics (EAS 1, EAS 2, and EAS 3), and differential absorption spectra with time delays between 0 and 300 ps, as well as time absorption profiles of (6,4)-, (6,5)-, (8,3)-, and (7,5)-SWCNTs are depicted in Figures 7 a–c, S38, and S39, respectively. In particular, all sets of differential spectra, that is, those of (6,5)-enriched SWCNTs, Rev-MINT-$\mathbf{1}_2$, and Rev-MINT-$\mathbf{2}_2$, are dominated by an immediate ground-state bleaching of the SWCNTs in the NIR-region (Figure S38, around 1000 nm). The latter finding mirror images the steady-state absorption spectra. Contributions from the exTTF-centered excited-state features in both MINTs, for example in the visible region, are masked by SWCNT-centered features. A closer look at the differential absorption spectra of (6,5)-enriched SWCNTs reveals minima at 464, 575, 664, 879, 997, and 1146 nm, while maxima appear at 485, 539, 616, 927, 1083, and >1200 nm.[26]

To investigate the chiral selectivity, kinetics of (6,5)-enriched SWCNTs, Rev-MINT-$\mathbf{1}_2$, and Rev-MINT-$\mathbf{2}_2$, were analyzed by single-wavelength analyses. Kinetics of the ground-state bleaching for (6,4)-, (6,5)-, (8,3)-, and (7,5)-SWCNTs yielded three different lifetimes, which differ for each chirality (see Table S6). In (6,5)-enriched SWCNTs, the two short-lived components are assigned to excited states, which stem from multiple exciton generations and interband–intertube relaxations, respectively, while the long-lived component relates to radiative exciton recombination.[27,28]

In Rev-MINT-$\mathbf{1}_2$ and Rev-MINT-$\mathbf{2}_2$, the short-lived component, which is due to higher excited states of the exTTF and SWCNTs, is only marginally impacted relative to (6,5)-enriched SWCNTs. In contrast, the intermediate-lived component is significantly shortened and is in good agreement with the strongest fluorescence quenching seen in the steady-state experiments. In general, features of the one-electron oxidized exTTF evolve as a rather broad positive absorption at around 700 nm. This is, however, a wavelength range that is dominated in Rev-MINT-$\mathbf{1}_2$ and Rev-MINT-$\mathbf{2}_2$ by ground-state bleaching of the S_{22} transitions. However, a weak positive broad signal is discernible in the spectra at ≈ 700 nm upon subtracting the SWCNT-centered contributions in Rev-MINT-$\mathbf{1}_2$ (dark blue) and Rev-MINT-$\mathbf{2}_2$ (light blue). We take this as evidence for the oxidation of exTTF (Figure S40), where the broad and positive absorptions are in line with the literature.[9c,31] In light of the aforementioned results, we interpret in Rev-MINT-$\mathbf{1}_2$, 1 ps for (6,4)-SWCNTs and 4 ps for (6,5)-SWCNTs as charge separation as well as 49 and 93 ps as charge recombination, respectively. In Rev-MINT-$\mathbf{2}_2$, charge separation occurs accordingly with 0.9 ps for (6,4)-SWCNTs and 4 ps for (6,5)-SWCNTs. This is followed by charge recombination with 197 and 78 ps, respectively.[29] For larger diameter (8,3)-SWCNTs, charge separation and charge recombination are, however, slower: 1 and 68 ps for the case of Rev-MINT-$\mathbf{1}_2$ and 0.6 and 68 ps for the case of Rev-MINT-$\mathbf{2}_2$. For the largest-diameter SWCNTs, namely (7,5)-SWCNTs, the lifetimes are essentially identical to those found in the (6,5)-enriched SWCNTs. Consequently, we postulate the absence of appreciable interactions/no interactions at all.

Photoexcitation of the exTTF moieties, which are mechanically interlocked onto pristine SWCNTs, resulted in the formation of an excited state, whose decay proceeds via a transient charge-separated state.[30] In the case of (6,5)-enriched SWCNTs, the two short-lived components and the

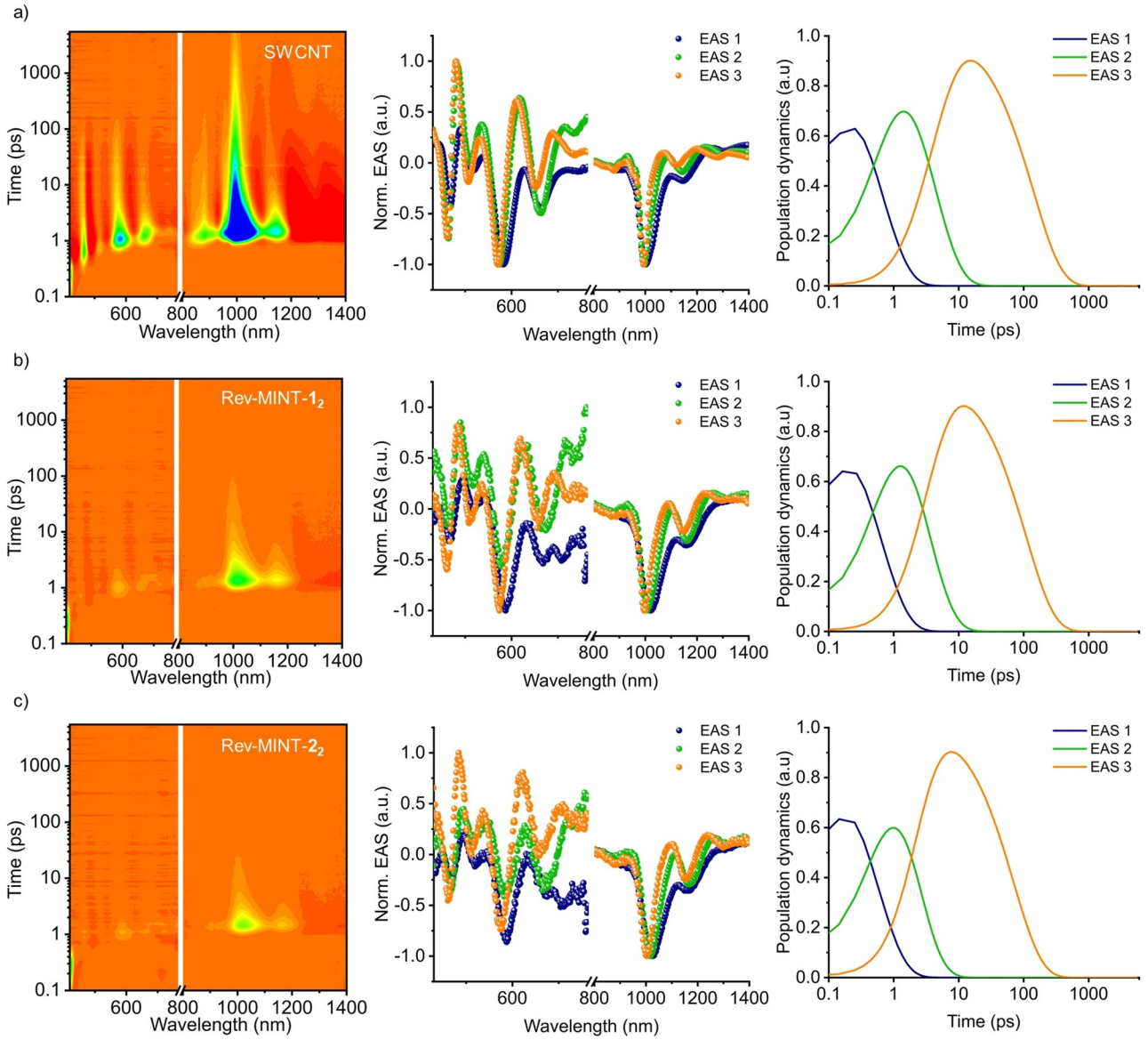

Figure 7. 3D-transient absorption spectra (intensities range from −0.015 to 0.002 counts) obtained upon femtosecond pump probe experiments following excitation with a 387 nm laser in D_2O/SDS (1 wt%) at rt: a) (6,5)-enriched SWCNTs, b) Rev-MINT-**1**$_2$, c) Rev-MINT-**2**$_2$ with corresponding deconvoluted evolution-associated spectra (EAS) and population dynamics of EAS 1, EAS 2, and EAS 3.

one long-lived component refer to the same as mentioned above. In MINTs, the short-lived and intermediate-lived components are characterized by a superimposition of simultaneously populated higher excited states of exTTF and SWCNTs (blue spectrum) and their relaxed excited states (green spectrum; Figure 7, EAS). The long-lived component (orange spectrum) relates to that of the charge-separated state, that is, oxidized exTTF and reduced SWCNTs.[9c,28,31] This conclusion is based on the fact that the long-lived component in Rev-MINT-**1**$_2$ and Rev-MINT-**2**$_2$ resembles the spectral feature in the 700 nm range upon subtracting the contribution of the (6,5)-enriched SWCNTs from both MINTs. This assists in verifying the formation of the one-electron-oxidized form of exTTF in Rev-MINT-**1**$_2$ and Rev-MINT-**2**$_2$. Accordingly, we assign the intermediate-lived component to charge separation. For the strongly quenched Rev-MINT-**2**$_2$, we gathered the shortest lifetimes of 0.5, 2, and 70 ps (see Table S7). Turning to the weakly quenched Rev-MINT-**1**$_2$, the lifetimes are 0.6, 3, and 109 ps. As such, the strongest fluorescence quenching goes hand-in-hand with the fastest excited-state decay.[32] Notable is the effect of the interlocked structure on the charge recombination, i.e. MINTs seemed to be faster than in the cases where exTTF macrocycles are noncovalently self-assembled onto SWCNTs.[31]

To summarize, the spectroscopic studies corroborate those conclusions that were made regarding the degree of functionalization for (6,5)-enriched SWCNTs. In particular, functionalization with exTTF macrocycles is facilitated by mutual electronic interactions. These are appreciably strong for the combination of (6,4)-SWCNTs with **1**$_2$ in Rev-MINT-**1**$_2$, whereas the larger (6,5)-SWCNTs are the ideal match for the larger **2**$_2$ in the Rev-MINT-**2**$_2$ samples.

Characterization by AFM and HR-TEM

While the bulk evidence discussed above has the advantage of being representative for the entire sample(s), we also aimed to provide state-of-the-art microscopic evidence for the mechanically interlocked structures. An initial investigation of Rev-MINT-$\mathbf{2_2}$ was carried out by atomic force microscopy (AFM). AFM topographic images were obtained upon spin-coating the MINT suspensions in methanol on HOPG (highly ordered pyrolytic graphite) substrates. Under optimized conditions, individualized SWCNTs were observed (see section 11 in the Supporting Information). The height profiles across a partially functionalized carbon nanotube were deemed particularly informative (Figure 8a,b). In the lowest contrast area of the AFM image, height profiles 1 and 2 represent the unfunctionalized part of the carbon nanotube with a height around 0.75 nm. In the interim region, height profiles around 1.5 nm are observed (height profiles 3 and 4),[33] which is in very good agreement with the calculated diameter of nanotube plus macrocycle, as long as the bulky exTTF groups are oriented parallel to the surface. In the image area of highest contrast (height profiles 5 and 6), the heights are in the range of 2.0 to 2.5 nm, which is in agreement with a very dense functionalization such that at least some macrocycles have to orient the bulky exTTF moieties perpendicular to the surface (see computational model in Figure 8b).

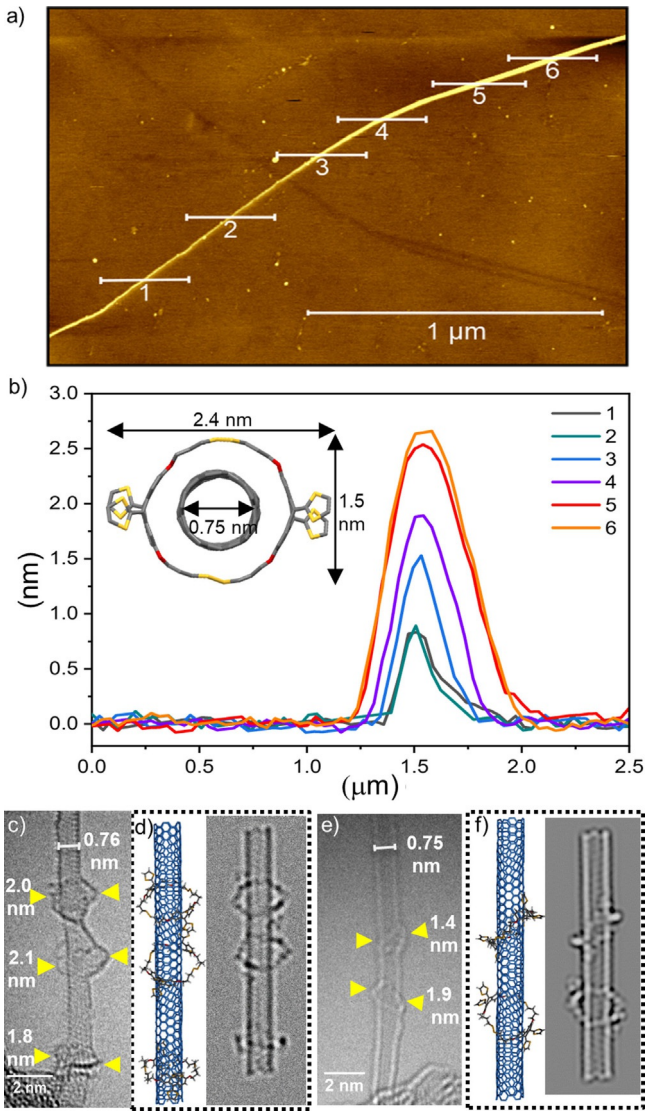

Figure 8. a) AFM topographic image of a spin-coated suspension of Rev-MINT-$\mathbf{2_2}$ in methanol on a HOPG substrate using the tapping mode. b) Corresponding height profile indicated in the AFM image; inset: calculated structure, which reveals the differences in diameters upon rotation. c) and e) HR-TEM images of Rev-MINT-$\mathbf{2_2}$ sample suspension in methanol drop cast on a Lacey carbon/Cu grid operated at 80 kV. d) and f) Corresponding HR-TEM simulations.

To visualize individual interlocked macrocycles around carbon nanotubes, selected MINT samples were analyzed by high-resolution transmission electron microscopy (HR-TEM). We drop-casted methanol suspensions of Rev-MINT-$\mathbf{2_2}$ samples on Lacey C-Cu grids (see section 12 in the Supporting Information). Besides large areas of bundled SWCNTs, we observed individual nanotubes featuring sections with distinct mechanically interlocked rings (Figure 8c,e and Figures S42). On some individual SWCNTs with a diameter of 0.75 nm, we observed rings in proximity, which is, to the best of our knowledge, an unprecedented result for MINT materials.[9–11] HR-TEM simulations (Figure 8d,f) revealed that the apparent diameter and visual appearance of the mechanically interlocked, relatively unsymmetric $\mathbf{2_2}$ macrocycles, strongly depends on the rotation and tilt angle of the rings with respect to the nanotube. For the simulated "scene" shown in Figure 8d,f, we observed a particularly good agreement between the observed and simulated images. Hence, the HR-TEM image with interlocked macrocycles on carbon nanotubes and the corresponding electron energy loss spectroscopy (EELS) data (Figure S43) unambiguously confirm the existence of mechanically interlocked macrocycles.

Conclusion

In this work, we introduce a new strategy for preparing mechanically interlocked SWCNT materials. Guided by computational modeling, we designed and synthesized two macrocycles that contain the curved π-extended TTF moiety as well as two disulfide bonds. The reversible opening and closing of these dynamic covalent bonds under mild basic conditions led to the functionalization of SWCNTs with mechanically interlocked rings, which according to rigorous TGA analyses make up ca. one third of the total weight in such "Rev-MINT" materials. A rough calculation based on the observed weight losses (section 14 in the Supporting Information) leads to an average distance of ca. 3 nm between interlocked macrocycles, which is in agreement with observations made by HR-TEM. Of note, the extensive decoration with rings allowed us to prepare stable suspensions of Rev-MINTs in THF.

In the context of prior work on MINT materials,[7l,9–11] the approach reported herein comes with two remarkable advantages: i) on a fundamental level, our dithiol building blocks allowed the comparative evaluation of three different types of

functionalization ("Rev", "Irrev", "Supra"). We found that both in respect to efficiency and robustness ("hot filtrations") the Rev-MINT approach was optimal, presumably because of error-correction during the formation of interlocked macrocycles. ii) On a more applied level, the disulfide bonds offer the attractive option of a quantitative reductive cleavage. We therefore envisage the opportunity to purify SWCNT mixtures by achieving diameter-selective solubilization in organic solvents, separating the most highly decorated SWCNT type by finely tuned ultracentrifugation and cleaving off the macrocycles.

Finally, we carried out comprehensive steady-state absorption, Raman and 3D-fluorescence spectroscopy studies, which demonstrated charge-transfer interactions between SWCNTs and exTTF macrocycles. Most importantly, the aforementioned methods provided evidence for the selective functionalization of smaller diameter (6,4)- and (6,5)-SWCNTs as opposed to the larger (7,5)- and (8,3)-SWCNTs, which also make up a significant proportion of the utilized (6,5)-enriched SWCNT starting material. As predicted by computational models, the observed chirality-selectivity differs for the two studied macrocycles, suggesting that it is due to a combination of size match and ground-state charge transfer.

Experimental Section

Representative procedure for the preparation of Rev-MINT samples: (6,5)-enriched SWCNTs (8 mg) were suspended in DMF (8 mL) by sonication (15 min). Macrocycles $\mathbf{1_2}$ or $\mathbf{2_2}$ (0.08 mmol), DBU (0.65 mmol), and DTT (0.01 mmol) were added and the mixture was sonicated for another 15 min. After stirring the mixture at room temperature for 72 h under inert atmosphere and in the absence of light, the suspension was filtered through a PTFE membrane (0.2 μm pore size). The solids were washed thoroughly with DCM and dried under vacuum (< 0.002 mbar) for further analysis.

Acknowledgements

We are grateful for financial support from the Deutsche Forschungsgemeinschaft (DFG, 182849149-SFB953 and 364549901-TRR 234), the University of Ulm, the DAAD (PhD fellowship to O.S.), and FAU Erlangen-Nürnberg. We thank Lionel Kroner for TGA measurements, Markus Wunderlin for MALDI-MS measurements, and Johannes Biskupek (Ulm) for recording EELS data. Open access funding enabled and organized by Projekt DEAL.

Conflict of interest

The authors declare no conflict of interest.

Keywords: curved π-systems · disulfide exchange · mechanically interlocked architectures · single-walled carbon nanotubes · supramolecular chemistry

[1] a) S. Iijima, *Nature* **1991**, *354*, 56 – 58; b) S. Iijima, T. Ichihashi, *Nature* **1993**, *363*, 603 – 605; c) D. S. Bethune, C. H. Kiang, M. S. de Vries, G. Gorman, R. Savoy, J. Vazquez, R. Beyers, *Nature* **1993**, *363*, 605 – 607.

[2] a) P. Avouris, Z. Chen, V. Perebeinos, *Nat. Nanotechnol.* **2007**, *2*, 605 – 615; b) S. Nanot, E. H. Hároz, J. H. Kim, R. H. Hauge, J. Kono, *Adv. Mater.* **2012**, *24*, 4977 – 4994; c) D. Son, J. H. Koo, J.-K. Song, J. Kim, M. Lee, H. J. Shim, M. Park, M. Lee, J. H. Kim, D.-H. Kim, *ACS Nano* **2015**, *9*, 5585 – 5593; d) Q. Cao, J. Tersoff, D. B. Farmer, Y. Zhu, S. J. Han, *Science* **2017**, *356*, 1369 – 1372; e) Y. Wen, N. Ares, F. J. Schupp, T. Pei, G. A. D. Briggs, E. A. Laird, *Nat. Phys.* **2020**, *16*, 75 – 82.

[3] a) X. Yu, J. Zhang, W. Choi, J.-Y. Choi, J. M. Kim, L. Gan, Z. Liu, *Nano Lett.* **2010**, *10*, 3343 – 3349; b) H. Omachi, T. Nakayama, E. Takahashi, Y. Segawa, K. Itami, *Nat. Chem.* **2013**, *5*, 572 – 576; c) J. R. Sanchez-Valencia, T. Dienel, O. Gröning, I. Shorubalko, A. Mueller, M. Jansen, K. Amsharov, P. Ruffieux, R. Fasel, *Nature* **2014**, *512*, 61 – 64; d) B. Liu, J. Liu, H.-B. Li, R. Bhola, E. A. Jackson, L. T. Scott, A. Page, S. Irle, K. Morokuma, C. Zhou, *Nano Lett.* **2015**, *15*, 586 – 595; e) B. Liu, F. Wu, H. Gui, M. Zheng, C. Zhou, *ACS Nano* **2017**, *11*, 31 – 53; f) J. Tomada, T. Dienel, F. Hampel, R. Fasel, K. Amsharov, *Nat. Commun.* **2019**, *10*, 3278.

[4] a) Y. Lin, S. Taylor, H. Li, K. A. S. Fernando, L. Qu, W. Wang, L. Gu, B. Zhou, Y.-P. Sun, *J. Mater. Chem.* **2004**, *14*, 527 – 541; b) D. Tasis, N. Tagmatarchis, A. Bianco, M. Prato, *Chem. Rev.* **2006**, *106*, 1105 – 1136; c) *Supramolecular Chemistry of Fullerenes and Carbon Nanotubes* (Eds.: N. Martin, J.-F. Nierengarten), Wiley-VCH, Weinheim, **2011**, chap. 10 – 12; d) A. Di Crescenzo, V. Ettorre, A. Fontana, *Beilstein J. Nanotechnol.* **2014**, *5*, 1675 – 1690; e) Y. Zhou, Y. Fang, R. P. Ramasamy, *Sensors* **2019**, *19*, 392; f) A. Venkataraman, E. V. Amadi, Y. Chen, C. Papadopoulos, *Nanoscale Res. Lett.* **2019**, *14*, 220.

[5] a) A. Bianco, M. Prato, *Adv. Mater.* **2003**, *15*, 1765 – 1768; b) Y. Zhang, J. Li, Y. Shen, M. Wang, J. Li, *J. Phys. Chem. B* **2004**, *108*, 15343 – 15346; c) F. Hauke, A. Hirsch in *Carbon Nanotubes and Related Structures: Synthesis Characterization, Functionalization and Applications* (Eds.: D. M. Guldi, N. Martin), Wiley-VCH, Weinheim, **2010**, pp. 135 – 179; d) N. Naidek, K. Huang, G. Bepete, M. L. M. Rocco, A. Pénicaud, A. J. G. Zarbin, E. S. Orth, *New J. Chem.* **2019**, *43*, 10482 – 10490.

[6] a) R. Chitta, A. S. D. Sandanayaka, A. L. Schumacher, L. D'Souza, Y. Araki, O. Ito, F. D'Souza, *J. Phys. Chem. C* **2007**, *111*, 6947 – 6955; b) F. D'Souza, O. Ito, *Chem. Commun.* **2009**, 4913 – 4928; c) "Noncovalent functionalization of carbon nanotubes": C. Backes, A. Hirsch, in *Chemistry of Nanocarbons* (Eds.: T. Akasaka, F. Wudl, S. Nagase), John Wiley & Sons, Chichester, **2010**, pp. 1 – 48; d) L. M. Arellano, M. Barrejon, H. B. Gobeze, M. J. Gomez-Escalonilla, J. L. G. Fierro, F. D'Souza, F. Langa, *Nanoscale* **2017**, *9*, 7551 – 7558; e) L. Liang, W. Xie, S. Fang, F. He, B. Yin, C. Tlili, D. Wang, S. Qiu, Q. Li, *J. Mater. Chem. C* **2017**, *5*, 11339 – 11368; f) S. Selmani, D. J. Schipper, *Chem. Eur. J.* **2019**, *25*, 6673 – 6692; g) M. Ji, M. L. Mason, D. A. Modarelli, J. R. Parquette, *Chem. Sci.* **2019**, *10*, 7868 – 7877.

[7] For interaction with oligomers/polymers, see: a) W. Yi, A. Malkovskiy, Q. Chu, A. P. Sokolov, M. L. Colon, M. Meador, Y. Pang, *J. Phys. Chem. B* **2008**, *112*, 12263 – 12269; b) D. Tuncel, *Nanoscale* **2011**, *3*, 3545 – 3554; c) J. López-Andarias, J. L. López, C. Atienza, F. G. Brunetti, C. Romero-Nieto, D. M. Guldi, N. Martín, *Nat. Commun.* **2014**, *5*, 3763; d) P. Bilalis, D. Katsigiannopoulos, A. Avgeropoulos, G. Sakellariou, *RSC Adv.* **2014**, *4*, 2911 – 2934; e) T. Fujigaya, N. Nakashima, *Sci. Technol. Adv. Mater.* **2015**, *16*, 024802; For interaction with DNA, see: f) J. F. Campbell, I. Tessmer, H. H. Thorp, D. A. Erie, C. Hill, N. Carolina, *J. Am. Chem. Soc.* **2008**, *130*, 10648 – 10655; g) Z. Li, Y.

Song, A. Li, W. Xu, W. Zhang, *Nanoscale* **2018**, *10*, 18586 – 18596; h) R. Nißler, F. A. Mann, P. Chaturvedi, J. Horlebein, D. Meyer, L. Vuković, S. Kruss, *J. Phys. Chem. C* **2019**, *123*, 4837 – 4847; i) Y. Zhang, F. Li, M. Li, X. Mao, X. Jing, X. Liu, Q. Li, J. Li, L. Wang, C. Fan, X. Zuo, *J. Am. Chem. Soc.* **2019**, *141*, 17861 – 17866; See for peptide-CNT interactions: j) G. R. Dieckmann, A. B. Dalton, P. A. Johnson, J. Razal, J. Chen, G. M. Giordano, E. Muñoz, I. H. Musselman, R. H. Baughman, R. K. Draper, *J. Am. Chem. Soc.* **2003**, *125*, 1770 – 1777; k) A. B. Dalton, A. Ortiz-Acevedo, V. Zorbas, E. Brunner, W. M. Sampson, S. Collins, J. M. Razal, M. Miki Yoshida, R. H. Baughman, R. K. Draper, et al., *Adv. Funct. Mater.* **2004**, *14*, 1147 – 1151; l) A. Ortiz-Acevedo, H. Xie, V. Zorbas, W. M. Sampson, A. B. Dalton, R. H. Baughman, R. K. Draper, I. H. Musselman, G. R. Dieckmann, *J. Am. Chem. Soc.* **2005**, *127*, 9512 – 9517; m) V. Z. Poenitzsch, D. C. Winters, H. Xie, G. R. Dieckmann, A. B. Dalton, I. H. Musselman, *J. Am. Chem. Soc.* **2007**, *129*, 14724 – 14732; n) C. Ge, J. Du, L. Zhao, L. Wang, Y. Liu, D. Li, Y. Yang, R. Zhou, Y. Zhao, Z. Chai, et al., *Proc. Natl. Acad. Sci. USA* **2011**, *108*, 16968 – 16973; o) N. Saifuddin, A. Z. Raziah, A. R. Junizah, *J. Chem.* **2013**, *2013*, 676815; p) E. Wu, M.-O. Coppens, S. Garde, *Langmuir* **2015**, *31*, 1683 – 1692; q) J. López-Andarias, S. H. Mejías, T. Sakurai, W. Matsuda, S. Seki, F. Feixas, S. Osuna, C. Atienza, N. Martín, A. L. Cortajarena, *Adv. Funct. Mater.* **2018**, *28*, 1704031.

[8] S. Mena-Hernando, E. M. Pérez, *Chem. Soc. Rev.* **2019**, *48*, 5016 – 5032.

[9] a) A. de Juan, Y. Pouillon, L. Ruiz-González, A. Torres-Pardo, S. Casado, N. Martín, Á. Rubio, E. M. Pérez, *Angew. Chem. Int. Ed.* **2014**, *53*, 5394 – 5400; *Angew. Chem.* **2014**, *126*, 5498 – 5504; b) A. López-Moreno, E. M. Pérez, *Chem. Commun.* **2015**, *51*, 5421 – 5424; c) E. Martínez-Periñán, A. de Juan, Y. Pouillon, C. Schierl, V. Strauss, N. Martín, Á. Rubio, D. M. Guldi, E. Lorenzo, E. M. Pérez, *Nanoscale* **2016**, *8*, 9254 – 9264; d) S. Leret, Y. Pouillon, S. Casado, C. Navío, Á. Rubio, E. M. Pérez, *Chem. Sci.* **2017**, *8*, 1927 – 1935; e) E. M. Pérez, *Chem. Eur. J.* **2017**, *23*, 12681 – 12689; f) L. De Juan-Fernández, P. W. Münich, A. Puthiyedath, B. Nieto-Ortega, S. Casado, L. Ruiz-González, E. M. Pérez, D. M. Guldi, *Chem. Sci.* **2018**, *9*, 6779 – 6784.

[10] R. Chamorro, L. De Juan-Fernández, B. Nieto-Ortega, M. J. Mayoral, S. Casado, L. Ruiz-González, E. M. Pérez, D. González-Rodríguez, *Chem. Sci.* **2018**, *9*, 4176 – 4184.

[11] K. Miki, K. Saiki, T. Umeyama, J. Baek, T. Noda, H. Imahori, Y. Sato, K. Suenaga, K. Ohe, *Small* **2018**, *14*, 1800720.

[12] M. Blanco, B. Nieto-Ortega, A. De Juan, M. Vera-Hidalgo, A. López-Moreno, S. Casado, L. R. González, H. Sawada, J. M. González-Calbet, E. M. Pérez, *Nat. Commun.* **2018**, *9*, 2671.

[13] a) A. R. Pease, J. O. Jeppesen, J. F. Stoddart, Y. Luo, C. P. Collier, J. R. Heath, *Acc. Chem. Res.* **2001**, *34*, 433 – 444; b) P. T. Corbett, J. Leclaire, L. Vial, K. R. West, J.-L. Wietor, J. K. M. Sanders, S. Otto, *Chem. Rev.* **2006**, *106*, 3652 – 3711; c) T. Takata, *Polym. J.* **2006**, *38*, 1 – 20; d) Y. Jin, C. Yu, R. J. Denman, W. Zhang, *Chem. Soc. Rev.* **2013**, *42*, 6634 – 6654.

[14] a) G. J. Bodwell, *Chem. Rec.* **2014**, *14*, 547 – 567; b) Y. Segawa, A. Yagi, K. Matsui, K. Itami, *Angew. Chem. Int. Ed.* **2016**, *55*, 5136 – 5158; *Angew. Chem.* **2016**, *128*, 5222 – 5245; c) "Curved π-Receptors": T. Matsuno, S. Sato, H. Isobe in *Comprehensive Supramolecular Chemistry II*, *Vol. 3* (Ed.:J. L. Atwood), Elsevier, Oxford, **2017**, pp. 311 – 328; d) G. Povie, Y. Segawa, T. Nishihara, Y. Miyauchi, K. Itami, *J. Am. Chem. Soc.* **2018**, *140*, 10054 – 10059; e) E. J. Leonhardt, R. Jasti, *Nat. Rev. Chem.* **2019**, *3*, 672 – 686; f) M. A. Majewski, M. Stępień, *Angew. Chem. Int. Ed.* **2019**, *58*, 86 – 116; *Angew. Chem.* **2019**, *131*, 90 – 122; g) Y. Xu, M. von Delius, *Angew. Chem. Int. Ed.* **2020**, *59*, 559 – 573; *Angew. Chem.* **2020**, *132*, 567 – 582.

[15] For reviews see a) F. G. Brunetti, J. L. López, C. Atienza, N. Martín, *J. Mater. Chem.* **2012**, *22*, 4188 – 4205; b) V. A. Azov, *Tetrahedron Lett.* **2016**, *57*, 5416 – 5425; For selected references on exTTFs as receptors see: c) E. M. Pérez, L. Sánchez, G. Fernández, N. Martín, *J. Am. Chem. Soc.* **2006**, *128*, 7172 – 7173; d) S. S. Gayathri, M. Wielopolski, E. M. Pérez, G. Fernández, L. Sánchez, R. Viruela, E. Ortí, D. M. Guldi, N. Martín, *Angew. Chem. Int. Ed.* **2009**, *48*, 815 – 819; *Angew. Chem.* **2009**, *121*, 829 – 834; e) D. Canevet, M. Gallego, H. Isla, A. de Juan, E. M. Pérez, N. Martín, *J. Am. Chem. Soc.* **2011**, *133*, 3184 – 3190; f) J. Calbo, A. de Juan, J. Aragó, J. Villalva, N. Martín, E. M. Pérez, E. Ortí, *Phys. Chem. Chem. Phys.* **2019**, *21*, 11670 – 11675.

[16] a) S. Otto, R. L. E. Furlan, J. K. M. Sanders, *J. Am. Chem. Soc.* **2000**, *122*, 12063 – 12064; b) B. Brisig, J. K. M. Sanders, S. Otto, *Angew. Chem. Int. Ed.* **2003**, *42*, 1270 – 1273; *Angew. Chem.* **2003**, *115*, 1308 – 1311; c) W. Zhou, H. Zheng, Y. Li, H. Liu, Y. Li, *Org. Lett.* **2010**, *12*, 4078 – 4081; d) L. I. James, J. E. Beaver, N. W. Rice, M. L. Waters, *J. Am. Chem. Soc.* **2013**, *135*, 6450 – 6455; e) S. Hamieh, V. Saggiomo, P. Nowak, E. Mattia, R. F. Ludlow, S. Otto, *Angew. Chem. Int. Ed.* **2013**, *52*, 12368 – 12372; *Angew. Chem.* **2013**, *125*, 12594 – 12598; f) S. P. Black, J. K. M. Sanders, A. R. Stefankiewicz, *Chem. Soc. Rev.* **2014**, *43*, 1861 – 1872; g) N. K. Pinkin, M. L. Waters, *Org. Biomol. Chem.* **2014**, *12*, 7059 – 7067.

[17] Our irreversible interlocking reference experiments ("Irrev-MINT") are related to earlier work by Dieckmann and co-workers, who irreversibly oxidized peptide-based dithiols in the presence of SWCNTs and provided limited evidence for mechanical interlocking. See Ref. [7j].

[18] At 420 °C, it can be assumed that the weight loss originates mainly from small molecules and is 95 % complete.

[19] a) Y. Maeda, K. Saito, N. Akamatsu, Y. Chiba, S. Ohno, Y. Okui, M. Yamada, T. Hasegawa, M. Kako, T. Akasaka, *J. Am. Chem. Soc.* **2012**, *134*, 18101 – 18108; b) M. Schirowski, G. Abellán, E. Nuin, J. Pampel, C. Dolle, V. Wedler, T.-P. Fellinger, E. Spiecker, F. Hauke, A. Hirsch, *J. Am. Chem. Soc.* **2018**, *140*, 3352 – 3360; c) M. Schirowski, F. Hauke, A. Hirsch, *Chem. Eur. J.* **2019**, *25*, 12761 – 12768.

[20] MINT samples were thoroughly dried overnight under high vacuum. For each analysis, equal amounts of sample were taken for TGA analysis ($\approx$1.5 mg). The results are averaged over three individual experiments.

[21] a) E. Moulin, G. Cormos, N. Giuseppone, *Chem. Soc. Rev.* **2012**, *41*, 1031 – 1049; b) Y. Jin, Q. Wang, P. Taynton, W. Zhang, *Acc. Chem. Res.* **2014**, *47*, 1575 – 1586; c) A. Fuhrmann, R. Göstl, R. Wendt, J. Kötteritzsch, M. D. Hager, U. S. Schubert, K. Brademann-Jock, A. F. Thünemann, U. Nöchel, M. Behl, S. Hecht, *Nat. Commun.* **2016**, *7*, 13623; d) R.-C. Brachvogel, M. von Delius, *Eur. J. Org. Chem.* **2016**, 3662 – 3670; e) *Dynamic Covalent Chemistry Principles, Reactions, and Applications* (Eds.: W. Zhang, Y. Jin), Wiley, Hoboken, **2018**.

[22] The small differences between recovered and pristine SWCNTs originate from the multiple chemical and mechanical treatments during the functionalization and defunctionalization procedures.

[23] (7,5)-SWCNTs features are not clearly visible in the NIR region of all samples.

[24] Normalization by means of using larger SWCNTs at lower wavenumbers are physically meaningless due to the restricted sizes of $\mathbf{1}_2$ or $\mathbf{2}_2$.

[25] A similar trend was also noted in the case of the 3D-NIR fluorescence spectra taken for CoMoCAT SWCNTs, which are prepared by a different method and feature a broader distribution of chirality signatures (CoMoCAT-Rev-MINT-$\mathbf{2}_2$ in Figure S37 c,d).

[26] Overall, the SWCNTs features are significantly red-shifted in both MINTs; minima are located at 469, 582, 667, 1014, 1160 nm, and 470, 587, 670, 1021, 1167 nm in the cases of Rev-MINT-$\mathbf{1}_2$ and Rev-MINT-$\mathbf{2}_2$, respectively. Maxima are found for Rev-MINT-$\mathbf{1}_2$ at 490, 544, 622, $>$1200 nm and for Rev-MINT-$\mathbf{2}_2$ at

490, 545, 631, >1200 nm. Some excited state features of the SWCNTs in both MINTs are not clearly visible.
[27] G. N. Ostojic, S. Zaric, J. Kono, M. S. Strano, V. C. Moore, R. H. Hauge, R. E. Smalley, *Phys. Rev. Lett.* **2004**, *92*, 117402 – 117405.
[28] A. Menon, Y. L. Slominskii, J. Joseph, O. P. Dimitriev, D. M. Guldi, *Small* **2020**, *16*, 1906745.
[29] No decrease was found for the (6,4)-SWCNTs long-lived component, which might be due to the macrocycle $\mathbf{2}_2$ being too large and flexible for the (6,4)-SWCNTs; clearly the flexible chiral selectivity toward the construction of the macrocycle around SWCNTs affects the lifetimes/interactions.
[30] Multiexponential global fittings were performed to fit the transient absorption spectra. A kinetic model, which was based on single wavelength analyses, with three components, yielded the most reasonable results (Table S7). In the 3D-transient spectra of (6,5)-enriched SWCNTs, Rev-MINT-$\mathbf{1}_2$, and Rev-MINT-$\mathbf{2}_2$, the relative intensities of the differential absorption features are well in line with the observations summarized in the steady-state absorption data.
[31] C. Romero-Nieto, R. Garcia, M. A. Herranz, C. Ehli, M. Ruppert, A. Hirsch, D. M. Guldi, N. Martin, *J. Am. Chem. Soc.* **2012**, *134*, 9183 – 9192.
[32] Our kinetic model yields lifetimes of 0.6, 4, and 140 ps for (6,5)-enriched SWCNTs.
[33] In the region of moderate functionalization density, the AFM tip (≈8 nm diameter) will encounter spaces where the distance between two rings is comparable or smaller than the tip diameter, which leads to further variation of observed heights.

Manuscript received: April 8, 2020
Accepted manuscript online: June 16, 2020
Version of record online: August 25, 2020

